3D Temporary-Magnetized Soft Robotic Structures for Enhanced Energy Harvesting

Liming Miao, Yu Song, Zhongyang Ren, Chen Xu, Ji Wan, Haobin Wang, Hang Guo, Zehua Xiang, Mengdi Han,* and Haixia Zhang*

The advent of functional materials offers tremendous potential in a broad variety of areas such as electronics, robotics, and energy devices. Magnetic materials are an attractive candidate that enable multifunctional devices with capabilities in both sensing and actuation. However, current magnetic devices, especially those with complex motion modalities, rely on permanently magnetized materials with complicated, non-uniform magnetization profiles. Here, based on magnetic materials with temporary-magnetization, a mechanically guided assembly process successfully converts laser-patterned 2D magnetic materials into judiciously engineered 3D structures, with dimensions and geometries ranging from mesoscale 3D filaments, to arrayed centimeter-scale 3D membranes. With tailorable mechanical properties and highly adjustable geometries, 3D soft structures can exhibit various tethered locomotions under the precise control of magnetic fields, including local deformation, unidirectional tilting, and omnidirectional rotation, and can serve as dynamic surfaces for further integration with other functional materials or devices. Examples demonstrated here focus on energy-harvesting systems, including 3D piezoelectric devices for noncontact conversion of mechanical energy and active motion sensing, as well as 3D solar tracking systems. The design strategy and resulting magnetic-controlled 3D soft structures hold great promise not only for enhanced energy harvesting, but also for multimodal sensing, robotic interfaces, and biomedical devices.

1. Introduction

Emerging soft microsystems attract huge attention in wearable biosensing,[1,2] biomedical implants,[3,4] human–machine interaction,[5,6] and energy conversion.[7–9] Unlike traditional large and rigid devices, soft microsystems commonly adopt functional materials with appealing properties, such as dielectric elastomers,[10] shape-memory polymers,[11] liquid metals,[12] and hydrogels.[13] Reliable actuation is of vital importance in microsystems, especially for energy harvesting, where the mechanical stability, controllability, and adaptability are highly desired to maintain the long-term power output in a complex environment. Recent advances in materials have enabled soft actuators with different driving mechanisms, including magnetic effect,[14] chemical effect,[15] photothermal effect,[16] and electrical effect.[17] The introduction of biomimetic designs or multidimensional geometries allows for the continuous operation in complex environments.[18–22] Among these strategies, the magnetic-controlled approach shows compelling advantages, due to its fast response, large deformation, precise control and stable repeatability.[23–25]

Magnetic materials deform under external magnetic fields, which is crucial for magnetic-controlled structures.[26–28] Most magnetic-controlled robotics exploit magnetic materials to achieve various locomotion, where the permanent and programmed magnetization profiles are key design parameters.[29] Strong magnetic fields from these permanent magnets pose a variety of incompatibility issues in scenarios such as electronic circuit, biomedicine, and micro/nanomanufacturing. By contrast, magnetic

L. Miao, Dr. Y. Song, Z. Ren, J. Wan, H. Wang, Z. Xiang, Prof. H. Zhang
National Key Lab of Nano/Micro Fabrication Technology
Institute of Microelectronics
Peking University
Beijing 100871, China
E-mail: hxzhang@pku.edu.cn
Dr. Y. Song
Department of Medical Engineering
Division of Engineering and Applied Science
California Institute of Technology
Pasadena, CA 91125, USA

The ORCID identification number(s) for the author(s) of this article can be found under https://doi.org/10.1002/adma.202102691.

C. Xu, H. Guo, Prof. H. Zhang
Academy for Advanced Interdisciplinary Studies
Peking University
Beijing 100871, China
Prof. M. Han
Department of Biomedical Engineering
College of Future Technology
Peking University
Beijing 100871, China
E-mail: hmd@pku.edu.cn

materials without permanent magnetization (e.g., soft magnetic materials, or magnetic materials with small coercivity) experience temporary magnetization under magnetic fields.[30] The removal of magnetic field can directly turn the magnetic domain distribution to its initial state without remanence. However, the lack of regionally programmed magnetization impedes the precise control and actuation modalities of planar magnetic structures under temporary magnetization. Recent exploration of 3D fabrication and functional material[31–34] enable a variety of 3D robotic structures with tailored engineering designs and provide feasible approaches to acquire 3D devices with specific properties and functions.[35–37]

Here we leverage a mechanically guided, compressive-buckling process to construct magnetic-controlled 3D robotic structures based on temporary-magnetized materials. A mixture of poly(dimethylsiloxane) (PDMS) and neodymium iron boron (NdFeB) microparticles forms a PDMS–NdFeB composite (PNC), which experiences temporary-magnetized process during the approach of an external magnetic field. The cooperation of the laser patterning and layer-by-layer transferring process allows for the preparation of various 3D robotic structures at different scales. The 3D robotic structures can realize different controlled locomotion, from unidirectional tilting to omnidirectional rotation under the precise control of the external magnetic field. Integration of energy materials and devices (i.e., piezoelectric materials, organic solar cells) to the 3D robotic structures yields advanced capabilities in energy harvesting. The action of external magnetic field and intrinsic elastic stress of the 3D robotic structure facilitate the complex and controllable deformation, showing promising prospects for enhanced multidirectional energy harvesting, as well as multifunctional sensing and multidimensional actuation.

2. Results and Discussion

2.1. Design of Magnetic-Controlled 3D Robotic Structures

The preparation of PNC film begins by mixing PDMS with NdFeB microparticles with different mass ratios at room temperature (**Figure 1**a; Figure S1, Supporting Information). In its initial state, the atomic force microscopy (AFM) images demonstrate that the PNC film exhibits random distribution of magnetic domains under zero-external magnetic field (Figure S2, Supporting Information). The approach of an external magnet to the PNC film induces magnetic field and converts the magnetic domains of the PNC film into oriented distribution with an obvious phase shift. And after the removal of the magnet, the temporary-magnetized PNC film can recover to its initial state (Figure S3, Supporting Information). The remanence (M_r) of the PNC film is highly dependent on the applied magnetic field, which is almost negligible under the unsaturated applied magnetic field (< 0.5 T) with low coercive force (H_C), while the M_r becomes much larger under the applied magnetic field over 0.5 T (Figure 1b; Figure S4, Supporting Information). The surface magnetic field of commonly commercial magnet is usually below 0.3 T and attenuates with the distance (Figure S5, Supporting Information). Therefore, it is reasonable to modulate the magnetic properties of PNC under the precise control of the external magnet.

The transformation from 2D PNC film to 3D robotic structure involves planar laser-patterning process and compressive-buckling process. First, a laser patterning process defines the obtained PNC film (200 µm in thickness) into various 2D patterns (left frame of Figure 1c). The corresponding scanning electron microscopy (SEM) images (right frame of Figure 1c) demonstrate the sharp boundaries of 2D precursors with different configurations, including straight lines, crisscross, and semicircular curves. As shown in Figure S6 (Supporting Information), the surface morphologies of laser-pattering process are strongly dependent on the power of laser and the mass ratio of the NdFeB microparticles. Both the cutting depth and cutting width increase with the power, and the power is determined at 8 W with the minimum line width of 200 µm to balance the width and depth of the laser-cutting notch. Meanwhile, the increased mass ratio of NdFeB microparticles leads to a decrease of the cutting depth caused by the increased energy loss. After transferring the patterned PNC 2D precursor on the prestretched elastomer substrate (Ecoflex 00-30, ≈400 µm in thickness), the adhesive layers (Dowsil 732 and silver adhesive, ≈65 µm in thickness) and stiffening layer (poly(ethylene naphthalate) (PEN), 125 µm in thickness) are successively screen-printed with alignment. The release of strain induces the compressive-buckling process and realizes the preparation of arrayed 3D robotic structures (left frame of Figure 1d and Figure S7 (Supporting Information)). The finite element analysis (FEA) results of the 3D table array further validates the conversion from planar patterns to 3D structures, where the low strain distribution of functional layers on the table top ensures the mechanical stability, and is beneficial to the practical applications (right frame of Figure 1d). The 3D robotic structure experiences locally deformations under the application of external magnet, and can easily recover to its initial state after the removal of magnet (Figure 1e). Compared with other technologies for building 3D structures, this strategy provides a reliable approach to develop magnetic-controlled 3D robotic structures at different scales, ranging from mesoscale ribbon, to sub-millimeter-scale single structure, and to large-scale arrayed structure (Figure S8, Supporting Information).

2.2. Characterization of PNC-Based 3D Robotic Structures

The prepared 2D PNC film shows great mechanical robustness under stretching, bending, and twisting states, and can be easily deformed with the attraction of a magnet (**Figure 2**a; Figures S9 and S10 (Supporting Information)). Both FEA and experimental results demonstrate that the magnetic force of 2D PNC film caused by the external magnet is about 1 mN, and it is critical to keep the gap lower than 4 mm to ensure a sufficient magnetic force for precise control (Figure S11, Supporting Information). In its initial state, the NdFeB microparticles, with random distribution of magnetic domains, are coated by a PDMS matrix in the PNC film, where no particle–particle magnetic interaction exists under the net-magnetic field. Based on theoretical and simulation analysis of 2D PNC model, the deformation of 2D PNC precursor mainly relies on two aspects: magnetic property and mechanical property, both of which can be determined by the mass ratio of NdFeB microparticles and the thickness
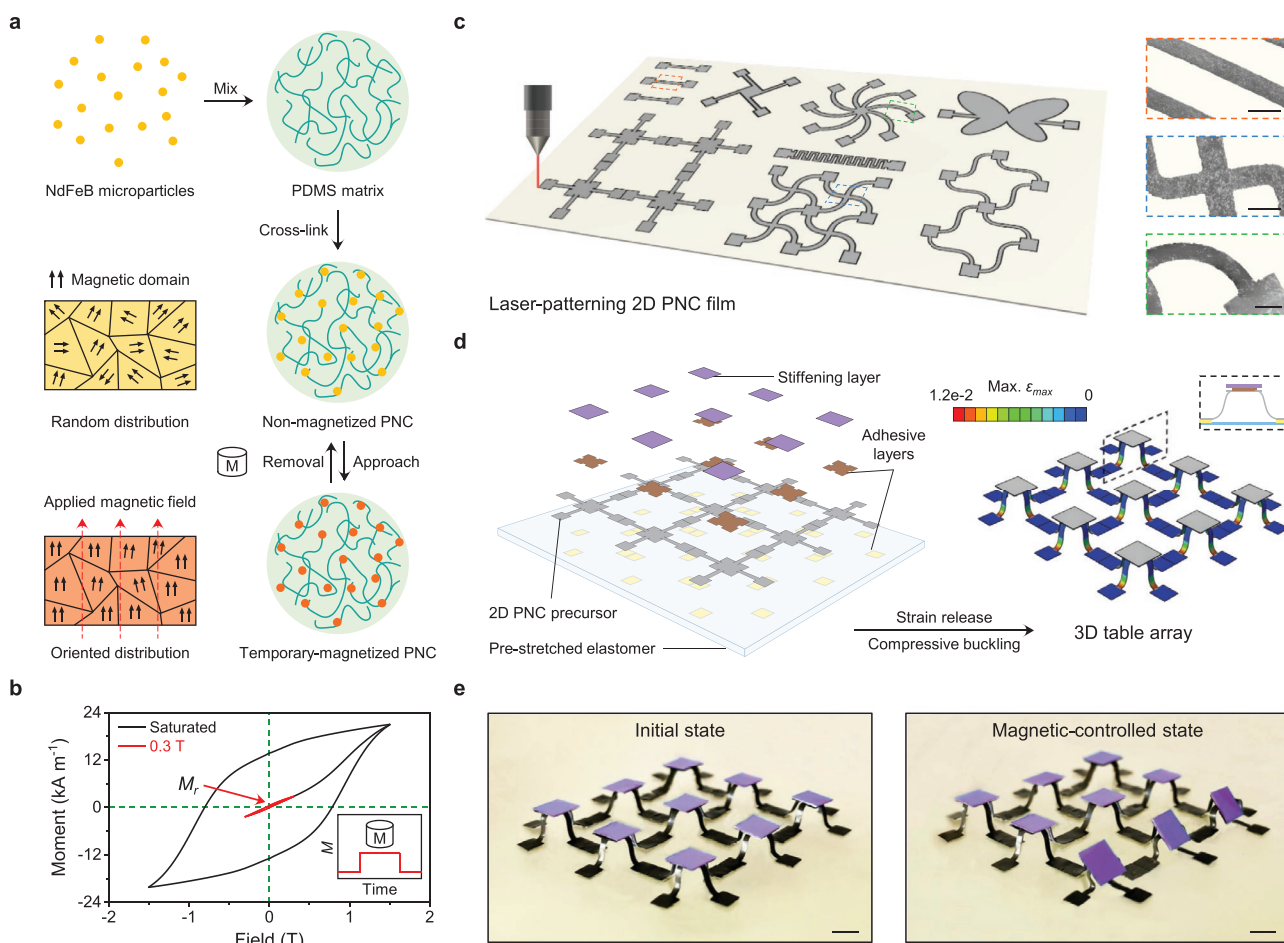
Figure 1. Magnetic-controlled 3D soft robotic structures. a) Schematic illustration of preparation process and temporary-magnetized behavior of PNC film. b) Static magnetic hysteresis loops of the PNC film under low and saturated magnetic fields. The inset shows the real-time magnetization response of the PNC film under the approach and removal of a magnet. c) Illustration of the laser-patterning 2D PNC film with tailored designs (left) and SEM images of the corresponding configurations (right). Scale bars: 500 μm. d) Illustration of a multilayered 2D precursor on a prestretched substrate (left) and finite element analysis (FEA) prediction of the 3D table array after strain release (right). Max. ε_{max}, the spatial maximum of the maximum principal strain. e) Optical images of the 3D table array under the initial state and magnetic-controlled state. Scale bars: 3 mm.

of PNC film, respectively (Note S1, Supporting Information). Adjusting the fabrication process can yield 2D PNCs with different parameters, showing controllable magnetic and mechanical properties (Figures S12 and S13, Supporting Information). First, to quantitatively evaluate the magnetic property, PNC film (200 μm in thickness) with different mass ratios of NdFeB microparticles are characterized. As the mass ratio of PDMS and NdFeB microparticles varies from 1:1 to 1:5, the bending stiffness correspondingly increases, and the movement (S) reaches maximum under the mass ratio of 1:3 (Figure 2b). The magnetization (M) increases correspondingly with the mass ratio (from 0.84 to 4.51 kA m^{-1} at 0.3 T) and larger applied magnetic field induces higher magnetization. Meanwhile, the increase of mass ratio also leads to a large shear modulus (G), indicating a stronger ability to resist deformation (Figure 2c). To achieve a balance between magnetic and mechanical properties, the following experiments select an optimal mass ratio of 1:3, as this value leads to the largest ratio between shear modulus and magnetism (M/G) (Figure 2d).

In addition, it is feasible to adjust the thickness (D) of 2D PNC film (from 100 to 300 μm) through the modulation of the rotation speed during the spin-coating process. A thicker PNC film produces larger bending stiffness (Figure 2e). Under a fixed magnetic field of 0.3 T, the magnetization also increases with the thickness of PNC film (from 1.20 to 4.17 kA m^{-1}, Figure 2f). The 2D PNC film (100 μm in thickness) with a larger critical parameter (M/D^2) demonstrates a larger movement during the deformation (Figure 2g). However, considering that the average diameter of NdFeB microparticles is ≈5 μm, thinner 2D PNC film possesses insufficient uniformity due to the influence of agglomeration. Therefore, 2D PNC films with the optimal thickness of 200 μm and mass ratio of 1:3 can provide satisfactory magnetic and mechanical properties, thereby serving as the reliable basic component for the following exploration.

Since the 2D PNC film shows limited modalities of deformation under the external magnetic field, 3D robotic structures with diverse geometries are developed to achieve magnetic-controlled and programmable locomotion. Through FEA-guided
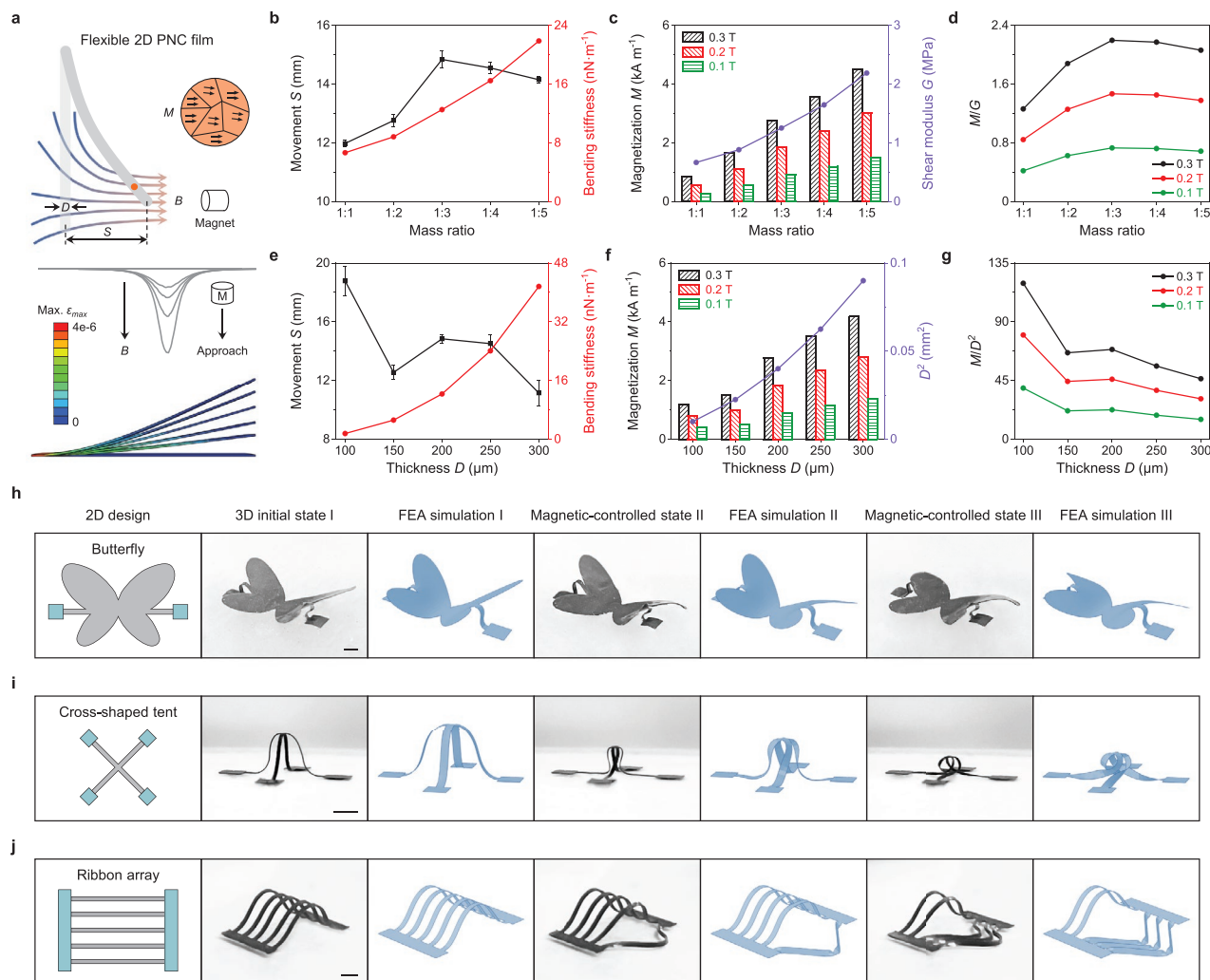
Figure 2. Characterization of PNC-based 3D robotic structures. a) Schematic illustration and simulated results of the deformation model of a 2D PNC film under the magnetic field of a cylindrical magnet. b) With the same thickness, the effect of mass ratio of NdFeB microparticles on the movement and bending stiffness of the 2D PNC film. The error bars are the standard error deviation from three measurements. c,d) Under different magnetic fields, c) effect of the mass ratio of NdFeB microparticles on the magnetization (M) and shear modulus (G) of the 2D PNC film, and d) the variation of M/G, a critical parameter that determines the degree of deflection for small deformation of the 2D PNC film. e) With fixed mass ratio of NdFeB microparticles, the effect of thickness on the movement and bending stiffness of the 2D PNC film. The error bars are the standard error deviation from three measurements. f,g) Under different magnetic fields, f) effect of the thickness on the M and corresponding dimension (D^2), and g) the variation of M/D^2, another critical parameter that determines the degree of deflection for small deformation of the 2D PNC film. h–j) Mechanically guided 2D precursors, optical images and FEA predictions of 3D robotic structures: h) butterfly, i) cross-shaped tent, and j) ribbon array, under initial and magnetic-controlled states. Scale bars: 2 mm.

structural design, the 2D PNC precursors on prestretched elastomer substrates are transformed into 3D robotic structures upon release of strain. These 3D robotic structures experience magnetic-controlled state under the external magnetic field and recover to initial state after the removal of the magnet (Figure S14, Supporting Information). In addition, when a small-scale magnet acts at different regions, the nonuniform distribution of magnetic field over the 3D structures allows for the diverse deformed modalities of 3D robotic structures. By modulating the acting regions of the magnet, the 3D robotic structures (butterfly, cross-shaped tent, and ribbon array) can demonstrate various distinct states, consistent with the corresponding FEA predictions (Figure 2h–j; Figure S15 and Video S1,

Supporting Information). For instance, controlling the movement direction of the magnet under the 3D butterfly enables the wings to flutter alternatively or synchronously. Through the simple and precise control of the magnet, it is feasible to realize more complex and functional deformations of the PNC-based 3D robotic structures. Similar to nonmagnetized NdFeB, soft-magnetic material (Fe) can also experience temporary-magnetized process with the approach of the external magnetic field. Through the general fabrication method with laser-cutting and mechanically guided compressive buckling process, the developed Fe-PDMS-based 3D robotic structures are able to demonstrate different magnetic-controlled states (Figure S16, Supporting Information). In contrast, the premagnetized NdFeB brings difficulty for 3D

ADVANCED
SCIENCE NEWS

www.advancedsciencenews.com

ADVANCED
MATERIALS

www.advmat.de
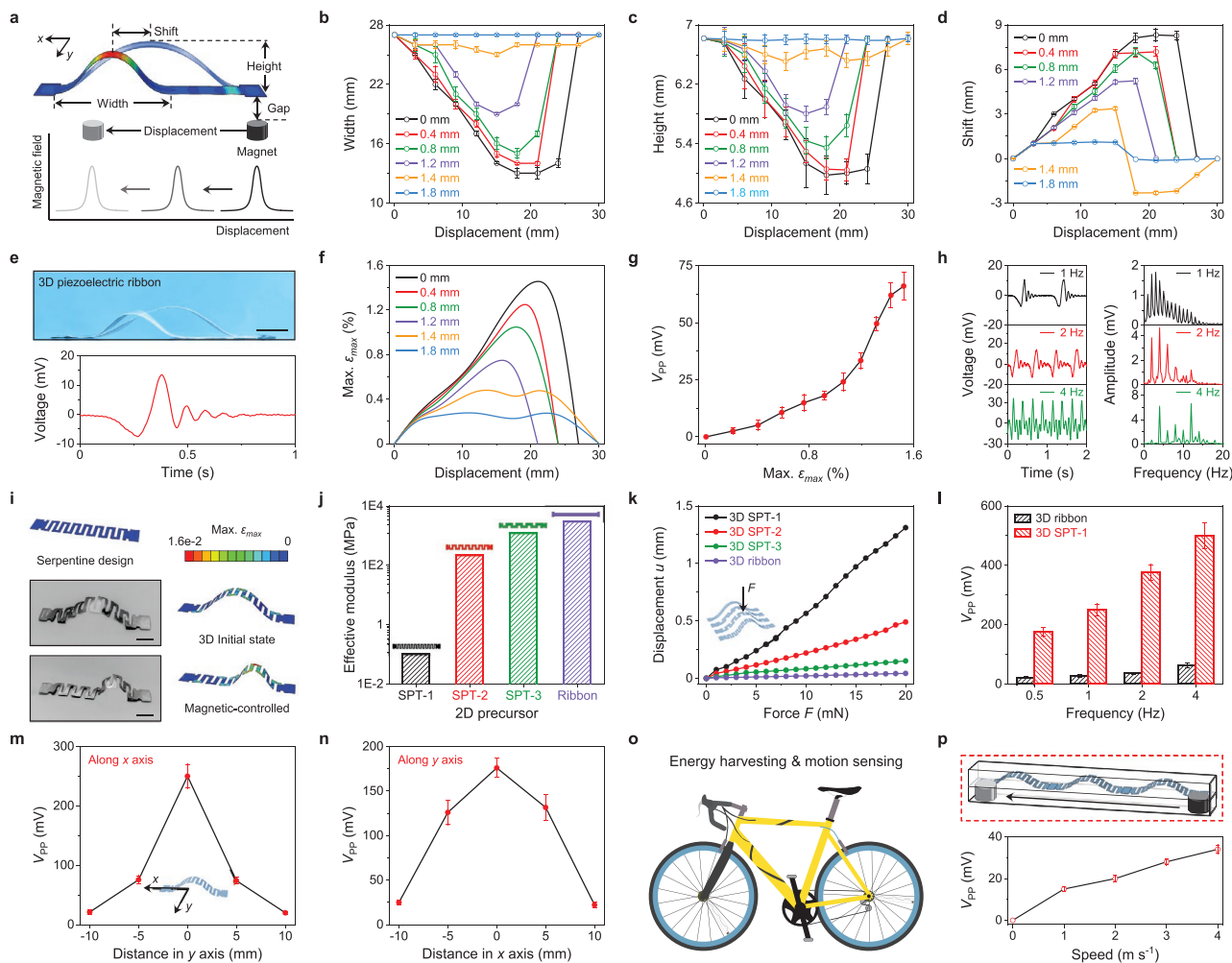
Figure 3. Magnetic-controlled energy harvesting from 3D piezoelectric structures. a) FEA result of strain distribution of the 3D ribbon under the magnetic field of a cylindrical magnet. b–d) Deformations of the 3D ribbon under the different gaps in z axis, when the magnet moves along the x axis: b) width, c) height, and d) shift. The error bars are the standard error deviation from three measurements. e) Optical image of the 3D piezoelectric ribbon under the initial and magnetic-controlled states and corresponding time-domain output voltage with the movement of a magnet. Scale bar: 5 mm. f) FEA results of the max. ε_{max} of 3D piezoelectric ribbon with the displacement of magnet along the x axis under the different gaps in z axis. g) Relationship between the output peak-to-peak voltage (V_{PP}) and max. ε_{max} of the 3D piezoelectric ribbon. The error bars are the standard error deviation from three measurements. h) Time-dependence output voltage of 3D piezoelectric ribbon at different operating frequencies (in the beginning 2 s of 8 s operating period) and corresponding fast Fourier transform (FFT) of whole operating period. i) Optical images and FEA results of strain distribution of 3D piezoelectric serpentine. Scale bars: 5 mm. j) Simulated results of effective modulus of different 2D precursors. k) Simulated results of the relationship between displacement and force to illustrate the ultralow stiffness feature of the 3D serpentine. l) The comparison of the frequency-domain output V_{PP} between the 3D ribbon and 3D SPT-1. The error bars are the standard error deviation from three measurements. m,n) Output V_{PP} of 3D SPT-1 with the in-plane movement of the magnet along the x axis (m) and the y axis (n) with different distances. The error bars are the standard error deviation from three measurements. o) Application of 3D piezoelectric serpentine for energy harvesting and motion sensing during biking. p) Schematic illustration of the magnetic-controlled piezoelectric harvester based on 3D serpentine array, and the correlation between the output V_{PP} and the biking speed. The error bars are the standard error deviation from three measurements.

robotic structures in both manufacturing and magnetic-controlled process (Figure S17, Supporting Information).

2.3. Magnetic-Controlled Energy Harvesting from 3D Piezoelectric Structures

For the basic 3D ribbon structure with a fixed width of 27 mm, the definition of parameters and the magnetic-controlled deformation appear in **Figure 3**a. During the movement of

the magnet from right to left, the cylindrical magnet forms a magnetic field, the center of which experiences synchronous shift. The magnetic field and its gradient act on a selectively working region of the 3D ribbon with a downward or obliquely downward magnetic force, inducing the corresponding part to collapse to the bottom (Figure S18, Supporting Information). Considering that the magnetic field is strongly related to the working distance along both in-plane and out-of-plane directions, it is feasible to investigate the magnetic-controlled process systematically with basic parameters, such as displacement,

**ADVANCED
SCIENCE NEWS**

www.advancedsciencenews.com

**ADVANCED
MATERIALS**

www.advmat.de

gap, and maximum magnetic field.[27] When the magnet moves along x axis, both the width and height (illustrated in Figure 3a) decrease with the displacement of magnet (Figure 3b,c). The increase of the gap between the 3D ribbon structure and the magnet in z axis (from 0 to 1.8 mm) attenuates the magnetic field. Under the strong magnetic field with the gap smaller than 1.2 mm, both the width and height of 3D ribbon structure dramatically decrease. Meanwhile, the shift of 3D ribbon structure increases with the displacement of the magnet (Figure 3d). The 3D ribbon structure recovers to its initial state at the accomplishment of the movement. In contrast, the weak magnetic field with a large gap allows for the small deformation of 3D ribbon, which experiences a reverse shift when the magnet acts on the left area with a right-downward force (Figure S19, Supporting Information). These results together demonstrate the diversity in motion modalities and provide a means to induce deformation of 3D structures in a remote, noncontact manner, with advantages in mitigating the mechanical damages.

In view of the advantages of noncontact deformation in robust mechanical energy harvesting, further development yields a 3D piezoelectric ribbon with a top electrode (silver, Ag, ≈3 µm in thickness), a polyvinylidene fluoride (PVDF) film (52 µm in thickness), a bottom electrode (Ag, ≈3 µm in thickness) and a PNC film (Figure 3e; Figure S20a, Supporting Information). During the mechanical motion of the external magnet, the 3D piezoelectric ribbon experiences deformation due to the magnetic attraction. The deformed 3D piezoelectric ribbon induces piezoelectric potential difference between the top and bottom electrodes. The process efficiently harvests mechanical energy and converts it into electrical energy (Figure S20b, Supporting Information). Both the mechanical structure and output voltage experience a slight damped oscillation during the recovery process. For the detailed evaluation of the specific 3D piezoelectric ribbon, the variation of gap (illustrated in Figure 3a) influences the relationship between spatial maximum of the maximum principal strain (max. ε_{max}) and the displacement of magnet (Figure 3f). According to the FEA results, with a small gap, the max. ε_{max} increases rapidly to reach the critical value, and decreases dramatically as the magnetic force is lower than the intrinsic elastic stress. While for the large gap, the max. ε_{max} increases slowly in the beginning, then the 3D structure shifts until the magnetic force is insufficient to support the deformation, leading to a symmetrical response. Obviously, large max. ε_{max} results in the enhanced peak-to-peak voltage (V_{PP}) of 66.56 mV at an operating frequency of 4 Hz, due to the strong magnetic field under small gap (Figure 3g). Figure 3h presents the time dependence of the output voltage in the first 2 s and corresponding fast Fourier transform (FFT) of the whole period (8 s) at different operating frequencies. Under the periodic movement of the magnet, the magnetic-controlled 3D piezoelectric ribbon demonstrates a low fundamental frequency. Multiple peaks in the FFT curves indicate strong nonlinear responses, offering opportunities in low-frequency energy harvesting. If the operating frequency is large than 4 Hz, the unfinished nonlinear oscillation of last cycle will overlap with the peak of the next cycle, changing the periodic signal and leading to the behavior with dual fundamental frequencies.

As discussed before, different mass ratios of NdFeB microparticles and thicknesses determine the magnetic and mechanical properties of the PNC film, which exerts an impact on the output performance. The prepared 3D piezoelectric ribbons with different parameters illustrate similar trends of V_{PP} under the varied frequencies ranging from 0.5 to 4 Hz, and show long-term output stability during the continuous operations (Figure S20c–e, Supporting Information). The above features are beneficial for periodically vibrational energy harvesting. To further optimize the structural design for enhanced output performance, 3D structures with ultralow effective stiffness are of interest. To meet the requirements for the compressive-buckling process and magnetic-controlled deformation, different serpentine patterns (linewidth: 1–3 mm) with low effective modulus and bending stiffness (F/u) are adopted for the development of 3D serpentine (Figure 3i–k; Figure S21, Supporting Information). The 3D serpentine with linewidth of 1 mm (3D SPT-1) demonstrates ultralow bending stiffness (14 mN mm^{-1}), typically more than one order of magnitude smaller than that of the 3D ribbon structure (476 mN mm^{-1}). It generates continuous piezoelectric output following the movement of the magnet with an amplitude (≈250 mV) 9 times higher than that of the 3D ribbon (≈27 mV) at an operating frequency of 1 Hz (Figure 3l). Independent to the temperature variation with minimum flux loss of NdFeB microparticles, 3D SPT-1 operates stably at different operating frequencies. The peak current reaches to around 2 µA and the maximum power is 0.16 µW at the load resistance of 25 MΩ, showing the reliability of energy harvesting (Figure S22, Supporting Information). Compared to other energy harvesting modes, the magnetic-controlled approach is more attractive for enhanced energy harvesting and motion sensing (Figure S23, Supporting Information). Meanwhile, compared to the coil unit-based electromagnetic generator (EMG) that relies on the Faraday induction, the 3D SPT-1 shows 20 times improvement in the amplitude of V_{PP}, which is suitable for practical applications with high signal-to-noise ratio (Figure S24, Supporting Information).

The 3D SPT-1 experiences different deformations when the magnet moves along the x and y axis. The corresponding output voltages under different lateral distance and longitudinal distance appear in Figure S25 (Supporting Information). At an operating frequency of 1 Hz, maximum outputs are obtained when the magnet moves along the center of the 3D serpentine (Figure 3m,n). Besides serpentine patterns, the 3D piezoelectric butterfly also demonstrates multiple motion modalities, and the piezoelectric output has strong dependence to the magnetic-controlled modes (Figure S26, Supporting Information). The magnetic-controlled 3D piezoelectric structure offers a solution for noncontact mode energy harvesting that mitigates mechanical damages, such as creases and scratches, enabling the long-term stability of the piezoelectric output (Figure S27, Supporting Information).

One compelling application is in the conversion of high-speed cyclic movement. Here, we integrate a magnet and a magnetic-controlled piezoelectric harvester based on 3D serpentine array to a bicycle wheel and the nearby supporting frame, respectively. The periodic rotation of wheel induces the back and forth movement of the magnet, leading to deformations of the 3D piezoelectric structure with continuous signal response (Figure 3o; Figure S28a, Supporting Information). The output V_{PP} of the 3D piezoelectric harvester is strongly dependent on
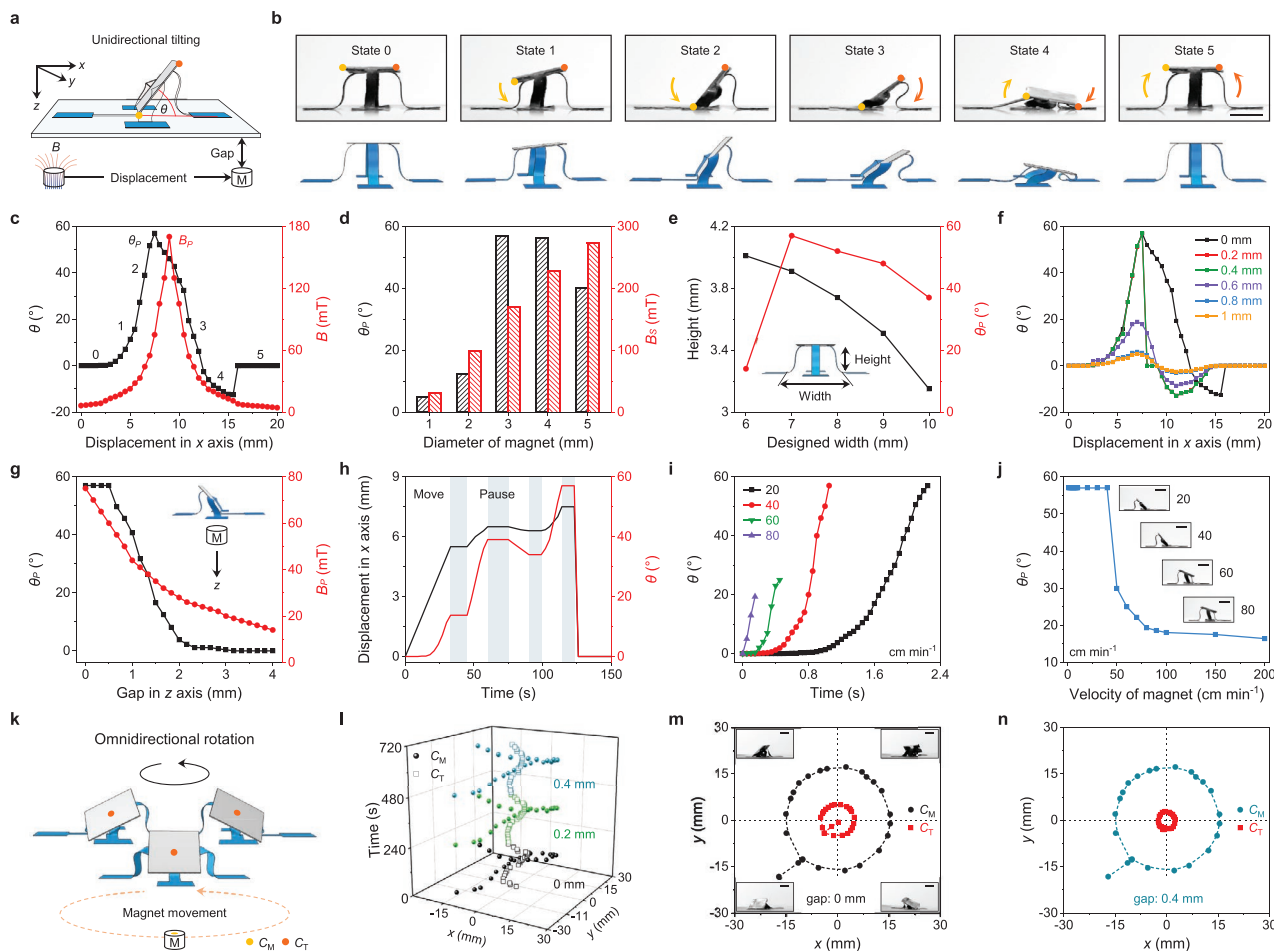
Figure 4. Magnetic-controlled 3D table. a) Schematic illustration of the unidirectional tilting of the magnetic-controlled 3D table. b) Optical images (top) and FEA predictions (bottom) of the magnetic-controlled 3D table with different states by moving a magnet along the x axis. Scale bar: 3 mm. c) The variation of tilting angle (θ) and magnetic field (B) with the displacement of the magnet along the x axis for in-plane control. d) Effect of the diameters of different cylindrical magnets on the θ_P and B_S. e) Effect of designed widths on the geometry and θ_P of the 3D table. f) The variation of tilting angle with the displacement of magnet along the x axis under the different gaps in the z axis. g) At the state where the tilting angle reaches θ_P, the variation of θ_P and B_P with the increasing gap of the magnet along the z axis for the out-of-plane control. h) Real-time step-less adjustment of tilting angle of the 3D table by moving a magnet along the x axis. i) The process of tilting angle of the 3D table to reach θ_P with different velocities of the magnet. j) Effect of velocity of the magnet on the θ_P with corresponding optical images of the 3D table. Scale bars: 3 mm. k) Schematic illustration of the omnidirectional rotation of the magnetic-controlled 3D table. C_M, center of the magnet. C_T, center of the 3D table top. l) Spatial coordinates of trajectory by the center of 3D table top and the magnet. m,n) The projective coordinates of trajectory by the center of 3D table top and the magnet with different gaps in the z axis of 0 mm (m) and 0.4 mm (n). Scale bars: 3 mm.

the speed of the bicycle. This feature provides additional opportunities in using the integrated 3D piezoelectric structure as an active sensor to detect the different operations of biking, such as acceleration, constant speed, and deceleration (Figure 3p; Figure S28b, Supporting Information). The exploration of judiciously engineered 3D piezoelectric structures with adjustable mechanical properties open avenues to realizing a unique and controllable energy conversion in a noncontact manner.

2.4. Magnetic-Controlled 3D Table-Based Solar Tracking System

As discussed before, 3D robotic structures have advantages in achieving complex and controllable deformations compared with the planar 2D films. A 3D table structure can realize the

unidirectional tilting easily with the in-plane control of the magnet (**Figure 4**a). The attached PEN stiffening layer on the top surface effectively avoids the curling of the 3D structure, and increases the tilting angle at the same time (Figure S29, Supporting Information). The moving magnet acts on the leg of 3D table structure at five distinct states with precise control (Figure 4b; Figure S30 and Video S2, Supporting Information). The defined tilting angle (θ) and magnetic field (B) are related to the displacement of the magnet in x axis. The 3D table maintains stable without the influence of the magnet at the beginning (state 0). The approach of a magnet induces the tilting of 3D table, while the tilting angle is relatively small due to the weak attraction (state 1). The tilting angle gradually increases with the strong magnetic force and reaches maximum (θ_P) when the left edge of the top surface touches the substrate

**ADVANCED
SCIENCE NEWS**

www.advancedsciencenews.com

**ADVANCED
MATERIALS**

www.advmat.de

(state 2). Then the right frame of the top surface starts to rotate downward, inducing a decrease of tilting angle (state 3). The increasing attraction of right table leg pulls the top surface backward and separates the left table leg from the substrate, forming a negative tilting angle (state 4). After the magnet moves away, the magnetic force is weaker than the elastic stress, and the 3D table structure recovers to its initial state rapidly (state 5). With this geometry, the tilting angle reaches maximum before the magnet moves to the center of the 3D table structure with a maximum magnetic field (B_P) (Figure 4c).

Besides, the diameter of the cylindrical magnet is also crucial to determine the magnetic field and the tilting angle. Small magnet has weaker magnetic field and large magnet results in lower spatial selectivity. A cylindrical magnet with a moderate diameter of 3 mm can induce the largest tilting angle (57°) with sufficient spatial magnetic field of the magnet (B_S) and satisfactory spatial selectivity, showing the potential for precise control and complex actuation (Figure 4d; Figure S31, Supporting Information). θ_P is a crucial parameter for the deformation of 3D table structure, and is intrinsically determined by the 3D geometry, associated with the precise modulation of prestretched process (Figure 4e; Figure S32, Supporting Information). With the increase of the designed width, the available θ_P decreases due to the limitation of the height. A moderate designed width (7 mm) is highly desired for the 3D table structure to obtain a large available θ_P, in order to facilitate the practical applications. During the lateral movement (the movement along the x or y axis) of the magnet, the gap in the z axis strongly influences the tilting process (Figure 4f; Video S3, Supporting Information). Due to the weak attraction of the magnet under a large gap (more than 0.6 mm), the 3D table first slightly tilts towards the left, then tilts to the right, leading to a symmetric response of tilting angle. In addition, when the tilting angle reaches maximum, the magnet can also subsequently move in the z axis as a way for out-of-plane control. The increased gap between the top surface of 3D table and the magnet attenuates the magnetic field and impels the 3D table to recover to its initial state (Figure 4g). For 3D table with larger width, the maximum tilting angle is smaller, while the lower height allows for larger magnetic force with longer recovering process (Figure S33, Supporting Information).

Under the periodic movement of the magnet, the 3D table operates reliably with long-term mechanical robustness and temperature stability (Figure S34, Supporting Information). It can realize continuous, step-less adjustment to follow the magnet moving and maintain the tilting angle during the pause of the magnet movement (Figure 4h). Meanwhile, the velocity of the magnet, corresponding to the rate of variation of magnetic field, is another critical factor to determine the magnetic-controlled movement. θ_P reaches maximum easily when the magnet moves with low velocity (from 1–40 cm min^{-1}), allowing the 3D table to balance intrinsic elastic stress with the magnetic force. When the magnet moves at high velocity (from 50 to 200 cm min^{-1}), the 3D table cannot experience full tilting process due to the rapid variation of external magnetic field, leading to a small θ_P with quick recovery (Figure 4i,j; Video S4, Supporting Information). In addition to the temporary-magnetized PNC film, exploiting soft magnetic materials (Fe-PDMS) is another strategy to develop magnetic-controlled 3D table.

However, due to the larger permeability, the Fe-PDMS-based 3D table immediately collapses with low controllability in tilting angle (Figure S35 and Video S5, Supporting Information). An ultra-small magnet is necessary for precise control of the Fe-PDMS-based 3D table, which inevitably increase the complexity of the movement. Besides, after the premagnetization of the PNC-based 3D table, it reversely tilts upon the approach of the magnet, and then rapidly collapses due to the large actuation strength, which is not suitable for precise control (Figure S36, Supporting Information).

Besides unidirectional tilting, it is feasible to realize omnidirectional rotation of the 3D table with the precise control of the magnet (Figure 4k; Figure S37 and Video S6, Supporting Information). The 3D table tilts first and rotates following the rotation of the magnet. In this case, the center of the 3D table top surface exhibits a circular trajectory. With a larger gap (0.4 mm) in the z axis, the magnetic force decreases, inducing a circular trajectory with smaller diameter (Figure 4l–n).

As we know, solar energy is one of important clean energy sources from environment,[38,39] and the real-time and step-less adjustment of incident angle with omnidirectional tracking is conductive to highly efficient solar-energy harvesting.[40,41] The capability in omnidirectional precise angle adjustment enables highly efficient solar-energy harvesting. As a demonstration, we integrate lightweight and mass-producible organic solar cells (OSC) on the top surfaces of a 3D table array to build a solar tracking system (**Figure 5**a). Compared with traditional MEMS technology-based micromotor unit for solar panel rotation, this 3D table-based solar tracking system shows several appealing features, including soft, re-configurable, and multi-scenario applicable, which are beneficial for the practical applications (Figure S38, Supporting Information). The OSC adopts an in-plane two-electrode configuration, which is compatible with the microelectronics fabrication process (Figure S39, Supporting Information). These OSC-integrated 3D tables also demonstrate two working modes (rotation and tilting), and the collected electrical signals are transmitted successfully through the four aluminum (Al)-coated table legs (Figure S40 and Video S7, Supporting Information). Based on the photovoltaic effect, the OSC is able to convert the light into electricity (Figure 5b; Note S2, Supporting Information). The output performance of OSC is strongly dependent on the incident angle of the external light. When charging a commercial capacitor of 22 μF with the OSC, both the charging speed and the maximum voltage attenuate with the decrease of the incident angle (Figure 5c). To realize effective and efficient solar energy harvesting, the 3D table-based solar tracking system with capabilities in real-time and precise control of the angle is highly desired (Figure S41, Supporting Information). With the optimized design of 3D table (7 mm in width), the output voltage and the photoelectric conversion efficiency (PCE) are much higher than those of the single OSC and other OSC-integrated 3D table (10 mm in width) at various incident angles (Figure 5d). Figure S42 (Supporting Information) illustrates the detailed working process. When the incident angle of external light shifts away from 90°, the performance of the OSC correspondingly decreases, exerting a trigger signal to the step motor of the magnetic-controlled system. The controller modulates the position of the magnet to change the shape of the 3D table with adjusted angle
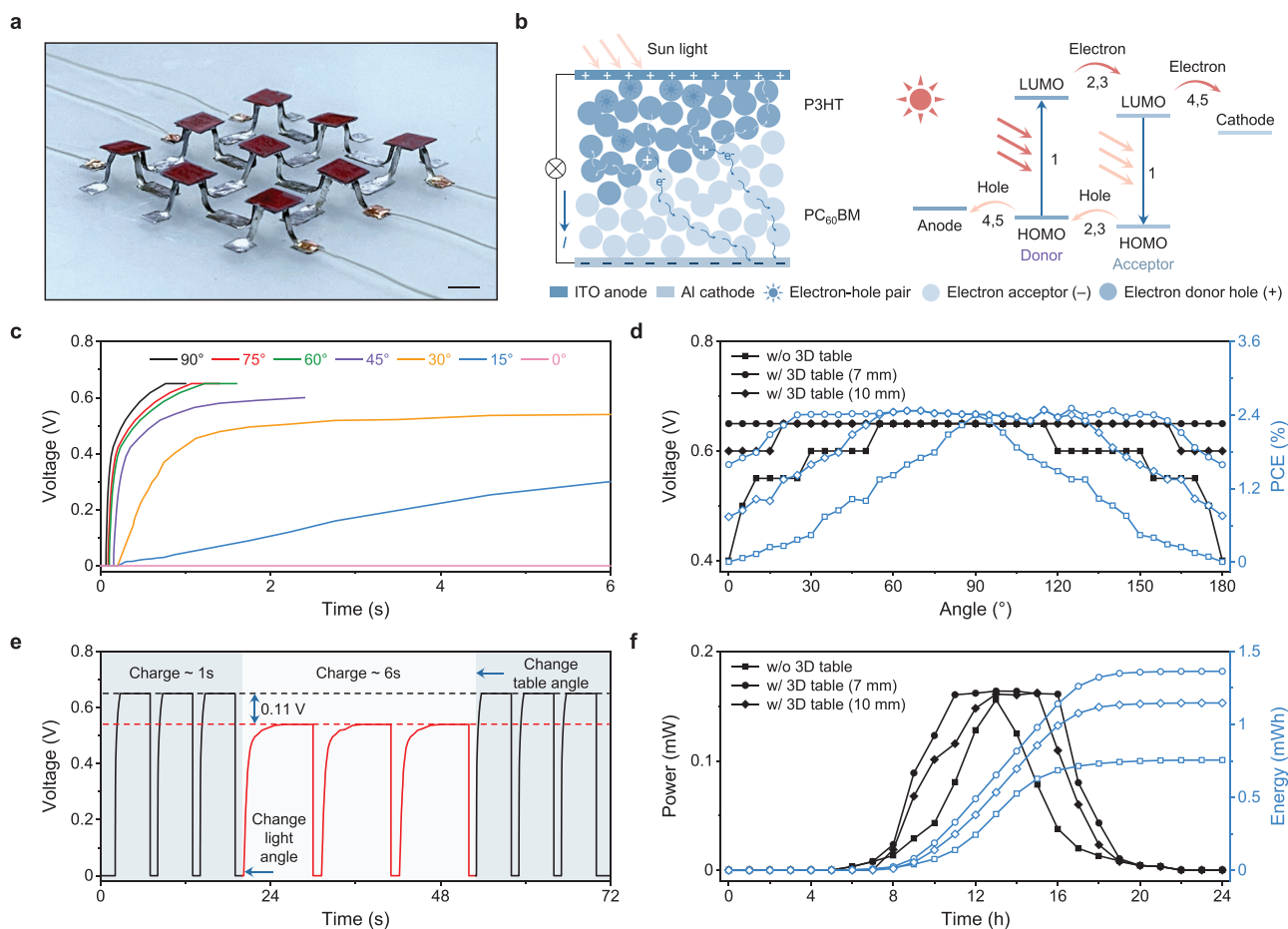
Figure 5. 3D table-based solar tracking system. a) Optical image of the OSC-integrated 3D table array. Scale bar: 5 mm. b) Schematic illustration and working mechanism of the OSC. c) The charging curves of a capacitor of 22 μF by the OSC under different incident angles. d) Enhanced output voltage and photoelectric conversion efficiency (PCE) of the magnetic-controlled 3D table-based solar tracking system with optimized design. e) The continuous charging–discharging curves of a capacitor of 22 μF by the OSC. The solar tracking system with magnetic-controlled dynamic adjustment of tilting angle follows the variation of incident angle. f) Enhanced power and stored energy of optimized 3D table-based solar tracking system during a 24 h simulated solar spectrum.

to maintain the power output. Under different incident angles, the OSC shows satisfying cycling stability when charging a capacitor continuously (Figure S43, Supporting Information). As the incident angle changes from 90° to 30°, the charging period becomes much longer (5 times) with reduced saturated voltage (0.11 V). Moving the magnet to an appropriate position changes the tilting angle of the 3D table to 60°, and improves the charging speed and the saturated voltage to its ideal state (Figure 5e). To further validate the enhanced solar energy harvesting, we adopt laboratory-level solar spectrum for 24 h to simulate the position of the solar light during a whole day. The 3D table-based solar tracking system with optimized design demonstrates satisfying power output and stores more energy within 24 h (Figure 5f), providing a feasible approach for continuous solar energy harvesting and power management.

3. Discussion

Robotic structures, with controllable and reliable deformations, are promising solutions for enhanced energy harvesting,

functional sensing, and precise actuation. The introduction of magnetic materials allows for the development of magnetic-controlled robotic structures. These structures usually adopt permanent magnetic materials that require specific treatment, such as regional programming of the magnetic domain. Here we demonstrate that robotic structures based on temporary-magnetized materials can also exhibit various magnetic-controlled states. The synergistic effect of magnetic materials with other functional materials can further inspire their features and broaden the applications.

Despite the promising prospects, current soft robotic structures face several major challenges. First, the limited engineering designs, functions and motion modalities of planar configurations hinder the variability, space utilization and integration level of robotic structures. Second, low-efficiency and inaccuracy inevitably occur during the development of optimal 3D structures due to the stress distribution and material adaptability. Third, conventional microfabrication process is not compatible with 3D manufacturing of flexible magnetic materials. Fourth, current research works mostly focus on the development of complex structures, while few attempts in exploring

practical applications, such as energy harvesting and active sensing.

Here, we address these challenges by exploiting a mechanically guided, mass-producible, compressive-buckling process to develop magnetic-controlled 3D robotic structures based on temporary-magnetized materials. The optimized mixture ratio of PDMS and NdFeB microparticles allows for the preparation of 2D PNC film with desired mechanical properties. Through the laser-patterning and compressive-buckling process, it is feasible to construct 2D PNC films into various 3D robotic structures with mechanically guided tailored designs at different scales. These structures can realize magnetic-controlled locomotion (local deformation, unidirectional tilting and omnidirectional rotation) under the precise control of an external magnet. The further integration with energy harvesters shows promising prospects for enhanced multidirectional energy harvesting. The 3D piezoelectric structure with judiciously engineered design provides a reliable approach for high-efficient energy conversion, and serves as an active sensor for motion sensing. The noncontact working mode greatly reduces the mechanical damages of the 3D piezoelectric structure and shows compelling advantages in terms of the stability, controllability, and adaptability for a long-term operation in complex environments. In addition, with the assistance of step-less and precise angle adjustment, the assembled 3D table-based solar tracking system, with biomimetic functions, facilitates the dynamic energy harvesting following the variation of incident angle of light. Therefore, these complex, 3D temporary-magnetized soft robotic structures empower an attractive strategy for enhanced energy harvesting, as well as multimodal biosensing, personalized therapy and human–machine interaction.

4. Experimental Section

Materials and Reagents: PDMS (Sylgard 184), silicon rubber (Dowsil 732), and Ecoflex 00-30 were purchased from Dow Corning. Neodymium iron boron (NdFeB) microparticles (5 μm diameter) were purchased from Magnequench International. Poly(vinylidene fluoride) film (PVDF, 52 μm in thickness) was purchased from Jingliang Electronics Co. Poly(ethylene naphthalene)/indium tin oxide (PEN/ITO, 125 μm in thickness) was purchased from Huanan Xiangcheng Technology Co. Magnets were purchased from Shenzhen Lala Magnet Material Co. $PC_{60}BM$, dichlorobenzene, and poly(3-hexylthiophene) (P3HT) were purchased from Solarmer Materials Inc. Silver adhesive glue was purchased from Hongkong Mechanic Co. Acetone and ethanol were purchased from Fisher Scientific. Polyimide film (PI, 13 μm in thickness) was purchased from HD MicroSystems Inc. Water-soluble tape (80 μm in thickness) was purchased from Jiaxing Zhongsha Co. PI tape (65 μm in thickness) was purchased from Shenzhen Sanwangda Electronics Materials Co.

Preparation of PNC Film: The preparation of PDMS–NdFeB composite (PNC) film started with the mixing of PDMS and NdFeB microparticles with different mass ratios (Figures S1 and S12a, Supporting Information). The mixture was then spin coated over the glass substrate for 40 s. The thickness of PNC film was dependent on the rotation speed of spin-coating process (Figures S12b and S13e, Supporting Information). It can be easily peeled off from the glass after fully cured at 80 °C for 1 h.

Fabrication of 3D Robotic Structures: To pattern the designed structure, a PNC film was attached onto a supporting substrate in a 50 W CO_2 laser cutter (Universal Laser System). The optimized parameters for the laser-patterning PNC film included power of 8 W, and speed of 10 mm s^{-1} (Figure S6, Supporting Information). The bonding sites of

the 2D patterned PNC precursor were selectively screen-printed with a layer of silicon rubber. After removal of the PI mask, the 2D PNC precursor was then transferred onto a prestretched elastomer with the assistance of water-soluble tapes. The release of the prestrain enabled the successful fabrication of various 3D robotic structures with a mechanically guided compressive-buckling process at different scales (Figure S8, Supporting Information). Meanwhile, with further selective screen-printing of another silver adhesive layer, the attached functional materials were applicable to various magnetic-controlled applications (Figure S7, Supporting Information). This fabrication process was also applicable for composite based on soft-magnetic materials, such as Fe-PDMS (Figures S16 and S35, Supporting Information).

Fabrication of 3D Piezoelectric Structures: The fabrication process began with laser-patterning of commercial film of PVDF film into designed ribbon serpentine and butterfly structures, followed by screen-printing Ag on both sides as electrodes (Figures S20a, S21, and S26, Supporting Information). The PNC mixture was then spin coated on the patterned PVDF film. During the curing process, the PVDF film was peeled off with half-cured PNC film, which served as a supporting layer. The obtained multilayer precursor was heated until the PNC film was fully cured, and transferred onto a prestretched elastomer substrate. After the release of prestrain, the 3D piezoelectric structure was prepared (Figure S21, Supporting Information). The serpentine design enabled the 3D PVDF structure with ultralow stiffness, and the geometrical parameters of the PNC film also determined the output performance.

Fabrication of Organic Solar Cells (OSC): The fabrication began with the ultrasonic bath-cleaning of anode (PEN/ITO film, 5 × 5 mm^2) in acetone (15 min), ethanol (15 min), and water (15 min). Then two strips of PI tape (1 mm in width) were laminated onto the PEN/ITO as hard masks and an additional layer MoO_3 (10 nm) was deposited under a high vacuum (1 × 10^{-5} Pa) for 2 min via vacuum evaporation deposition. Next, an ultraviolet-light-emitting diode (UV-LED) light source irradiation machine (Shenzhen Sankun Technology Co.) implemented UV hydrophilic treatment on the surface of MoO_3 layer for 15 min. After the mixture of P3HT:$PC_{60}BM$ (10 mg mL^{-1}:10 mg mL^{-1}) was dissolved in dichlorobenzene (2 wt%) and stirred at 40 °C for 48 h, it was further spin coated onto the surface of MoO_3 layer at 2000 rpm for 1 min and heated at 150 °C for 15 min. Followed by the removal of one strip of PI tape, an Al layer (150 nm in thickness) was deposited on the active layer at a rate of 0.25 nm via sputtering process to form Al cathode and another Al layer deposited on the ITO layer serves the anode. The planar OSC was successfully developed after removing the other strip of PI tape (Figure S39, Supporting Information).

Fabrication of 3D Table with OSC: Based on the laser-patterning process to develop 2D table structure, an Al layer (100 nm in thickness) was selectively deposited on four table legs as conductive pads via sputtering process. The top surface of the table was then screen-printed with a layer of silver adhesive, in alignment with the attached two Al electrodes of the OSC (Figure S40, Supporting Information). After curing the silver adhesive for 5 min, the fabrication and transfer of 2D precursor with OSC followed the procedures for 3D robotic structure described above. The releasing of the prestretched silicone elastomer enabled OSC-integrated 3D table for magnetic-controlled solar tracking system.

Measurement of the Magnetic Properties of PNC Film: The magnetic properties of PNC film with different parameters (different mass ratios of NdFeB microparticles, and different thicknesses) were evaluated by measuring the static magnetic hysteresis loops through an alternating gradient magnetometer (PMC MicroMag 2900-04C) at room temperature (25 °C). The detailed testing parameters for the magnetic hysteresis loops are listed in Table S1 (Supporting Information). Before the measurement, the PNC film was cut into 2 × 2 mm^2 pieces to fit the sample holder size of the magnetometer. At different applied external magnetic fields, the susceptibility, the remanence, and the magnetic moment were acquired from the corresponding static magnetic hysteresis loops (Figures S4 and S13, Supporting Information). The phase distribution of magnetic domains of the PNC film was measured by atomic force microscope (AFM, BRUKER Inc.) with the magnetic

probe (Figures S2 and S3, Supporting Information), and was acquired through commercial AFM software Nanoscope Analysis 13.0.

Measurement of the Mechanical Properties of PNC Film: The thickness of PNC film was measured through a thickness gauge (THI-1801), and the corresponding strain–stress curves were evaluated through an auto tensile tester (Labthink C610M) under the pulling speed of 10 mm min^{-1} (Figure S13a, Supporting Information). The dimensions of the samples, the pulling area and two clamping area were 15×70, 15×50, and 15×10 mm^2, respectively.

Characterization of 3D Robotic Structures: The surface morphologies of both 2D PNC films and developed 3D robotic structures with different parameters were acquired using scanning electron microscopy (SEM, Quanta 600 F, FEI Co.) and single lens reflex camera (SLR, Nikon D7100). By measuring the surface magnetic field of a fixed point through a gauss meter (HFBTE TD8620), the applied external magnetic field of a magnet can be evaluated (Figure 4c,d; Figure S18, Supporting Information). The movement of the 2D PNC film under the magnetic field of a magnet with a working distance of 5 mm was obtained by computer aided measuring of the front view of optical images by the SLR camera. The temperature variation was modulated through a ceramic hot plate (Thermo Scientific) and the real-time readings of temperature were acquired from an infrared thermometer (Lasergrip 800, Etekcity Inc.) to evaluate the effect of temperature on performance of various 3D robotic structures (Figures S22e and S34b, Supporting Information).

Magnetic-Controlled System for 3D Robotic Structures: To realize accurate deformation and precise control of 3D robotic structures, the magnetic-controlled system consisted of a step motor (NEMA 17HS3401-A), three proximity switch sensors (SN04-N), a step motor driver (TB 6600), a rotary encoder (HN3806-AB-600N), and a programmer single-axis controller (DKC-Y110). With the designed mechanical structure, the magnet was able to move freely in any directions to modulate the magnetic-controlled deformation of the 3D robotic structures (Figures S15, S31, S33, Supporting Information). In addition, during the movement of the magnet, the velocities can be manually set by the controller, ranging from 0.1 to 200 cm min^{-1} (Figure 4i,j). To meet the requirements of different applications, the magnetic-controlled system demonstrated two programmed working modes with continuous and intermittent sliding (Figure 4c,h).

Measurement of 3D Piezoelectric Structures for Energy Harvesting: The data acquisition system included a magnet, the prepared 3D piezoelectric structures, a magnetic-controlled system, and a digital oscilloscope (Agilent DSO-X 2014A). The movement of the magnet was programmed with the magnetic-controlled system to produce periodic variation of magnetic field at frequencies from 0.5 to 4 Hz. The magnetic-controlled dynamic deformation of 3D piezoelectric structures can effectively convert mechanical energy into electrical energy (Figure S20b, Supporting Information). The digital oscilloscope was adopted to record the output voltage, output current and corresponding maximum power of various 3D piezoelectric structures under different energy harvesting modes and coil unit-based EMG (Figures S22–S28, Supporting Information).

Measurement of 3D Table-Based Solar Tracking System for Energy Harvesting: For the measurement of OSC, the semiconductor parameter analyzer (Keithley 4200A) measured the responses of current-voltage (*I–V*) behavior with peak power, open-circuit voltage and short-circuit current over a voltage range from −1 to 1 V. Then the power, energy, and other parameters were calculated based on the acquired *I–V* curves. A solar simulator (Newport 91160, AM 1.5 G, 100 mW cm^{-2}) was adopted to produce the simulated solar spectrum. With the dynamic modulation of incident angle of the light, it was possible to evaluate the performance of the single OSC and 3D table-based solar tracking system for energy harvesting under different incident angles (Figure S41, Supporting Information). The solar tracking system consisted of the OSC-integrated 3D table, magnetic-controlled system, simulated solar spectrum and the external circuit module. For the detailed working process, the shift of the incident angle of the external light attenuates the charged voltage of the capacitor. With the real-time monitoring of the charging capability, the circuit module then exerted a trigger signal to the magnetic-controlled system allowing the movement of the magnet to an optimal position. The adjustment of tilting angle of 3D table under the correspondingly magnetic-controlled state enables the modulation of the incident angle to maintain the high output performance (Figure S42, Supporting Information). Meanwhile, a digital oscilloscope recorded the real-time charging curves of commercial capacitors by solar tracking system with long-term stability (Figure S43, Supporting Information).

Finite Element Analysis (FEA) of 3D Robotic Structures: For all the mechanically guided patterns designed, FEA predictions demonstrated the transform from 2D precursors to the corresponding 3D robotic structures under different states by using commercial FEA software ABAQUS 6.14 (Figures S8 and S14, Supporting Information). Based on the experimental results, the simulation adopted the following parameters of 2D PNC film with the thickness of 200 µm, the mass ratio of PDMS to NdFeB microparticles (1:3), the elastic modulus (*E*) of 3.6 MPa, and the Poisson's ratio (*v*) of 0.49 (Figure S13, Supporting Information). The obtained 3D mesh was then imported into commercial computer aided engineering (CAE) software Hypermesh 14.0 to rebuild the entity of 3D structure. After the importation of 3D entity into commercial software Ansoft Maxwell 16, the magnetic field of the magnet, magnetization of PNC-based 3D structure, and the distribution of magnetic force were analyzed (Figures S4, S11, S30, S36, Supporting Information). Under low magnetic field, the static magnetic hysteresis loops demonstrated almost across the original point with ignored coercive force (H_C), and the experimentally measured magnetic permeability ($\chi = 9.2$ kA m^{-1} T^{-1}) of PNC film was adopted for the simulation. The FEA results of the distribution of magnetic force was imported into the ABAQUS again for the mechanical analysis to acquire the deformation of 3D robotic structures with corresponding strain distribution (Figures S19 and S21, Supporting Information).

In addition, the FEA simulation of generated potential of 3D piezoelectric structures was conducted by the commercial software COMSOL Multiphysics 5.5 under the magnetic-controlled deformation (Figure S20b, Supporting Information). According to the theoretical analysis,[42] the output voltage of piezoelectric energy harvester was strongly related to the applied strain. During the periodic movement of the magnet, the increasing magnetic field of the magnet induced the large strain of the magnetic-controlled 3D piezoelectric structures, thus demonstrating an attractive capability for enhanced energy harvesting (Figure S23, Supporting Information).

Supporting Information

Supporting Information is available from the Wiley Online Library or from the author.

Conflict of Interest

The authors declare no conflict of interest.

Author Contributions

L.M and Y.S. contributed equally to this work. H.Z., L.M. and Y.S. initiated the concept. L.M., Y.S., Z.R., C.X., and M.H. designed the experiments; L.M. and Y.S. led the experiments and collected the overall

**ADVANCED
SCIENCE NEWS**

www.advancedsciencenews.com

**ADVANCED
MATERIALS**

www.advmat.de

[1] J. Kim, A. S. Campbell, B. E. de Avila, J. Wang, *Nat. Biotechnol.* **2019**, *37*, 389.

[2] Y. Yang, W. Gao, *Chem. Soc. Rev.* **2019**, *48*, 1465.

[3] M. Cianchetti, C. Laschi, A. Menciassi, P. Dario, *Nat. Rev. Mater.* **2018**, *3*, 143.

[4] J. Koo, M. R. MacEwan, S. K. Kang, S. M. Won, M. Stephen, P. Gamble, Z. Xie, Y. Yan, Y. Y. Chen, J. Shin, N. Birenbaum, S. Chung, S. B. Kim, J. Khalifeh, D. V. Harburg, K. Bean, M. Paskett, J. Kim, Z. S. Zohny, S. M. Lee, R. Zhang, K. Luo, B. Ji, A. Banks, H. M. Lee, Y. Huang, W. Z. Ray, J. A. Rogers, *Nat. Med.* **2018**, *24*, 1830.

[5] C. M. Boutry, M. Negre, M. Jorda, O. Vardoulis, A. Chortos, O. Khatib, Z. Bao, *Sci. Rob.* **2018**, *3*, eaau6914.

[6] Q. Hua, J. Sun, H. Liu, R. Bao, R. Yu, J. Zhai, C. Pan, Z. L. Wang, *Nat. Commun.* **2018**, *9*, 244.

[7] Y. Song, J. Min, Y. Yu, H. Wang, Y. Yang, H. Zhang, W. Gao, *Sci. Adv.* **2020**, *6*, eaay9842.

[8] J. Chen, Y. Huang, N. Zhang, H. Zou, R. Liu, C. Tao, X. Fan, Z. L. Wang, *Nat. Energy* **2016**, *1*, 16138.

[9] M. Han, H. Wang, Y. Yang, C. Liang, W. Bai, Z. Yan, H. Li, Y. Xue, X. Wang, B. Akar, H. Zhao, H. Luan, J. Lim, I. Kandela, G. A. Ameer, Y. Zhang, Y. Huang, J. A. Rogers, *Nat. Electron.* **2019**, *2*, 26.

[10] E. Acome, S. K. Mitchell, T. G. Morrissey, M. B. Emmett, C. Benjamin, M. King, M. Radakovitz, C. Keplinger, *Science* **2018**, *359*, 61.

[11] A. Lendlein, O. E. C. Gould, *Nat. Rev. Mater.* **2019**, *4*, 116.

[12] Z. Ma, Q. Huang, Q. Xu, Q. Zhuang, X. Zhao, Y. Yang, H. Qiu, Z. Yang, C. Wang, Y. Chai, Z. Zheng, *Nat. Mater.* **2021**, *20*, 859.

[13] H. W. Huang, M. S. Sakar, A. J. Petruska, S. Pane, B. J. Nelson, *Nat. Commun.* **2016**, *7*, 12263.

[14] S. Tasoglu, E. Diller, S. Guven, M. Sitti, U. Demirci, *Nat. Commun.* **2014**, *5*, 3124.

[15] M. Z. Miskin, A. J. Cortese, K. Dorsey, E. P. Esposito, M. F. Reynolds, Q. Liu, M. Cao, D. A. Muller, P. L. McEuen, I. Cohen, *Nature* **2020**, *584*, 557.

[16] S. Wang, Y. Gao, A. Wei, P. Xiao, Y. Liang, W. Lu, C. Chen, C. Zhang, G. Yang, H. Yao, T. Chen, *Nat. Commun.* **2020**, *11*, 4359.

[17] K. Y. Ma, P. Chirarattananon, S. B. Fuller, R. J. Wood, *Science* **2013**, *340*, 603.

[18] G. Li, X. Chen, F. Zhou, Y. Liang, Y. Xiao, X. Cao, Z. Zhang, M. Zhang, B. Wu, S. Yin, Y. Xu, H. Fan, Z. Chen, W. Song, W. Yang, B. Pan, J. Hou, W. Zou, S. He, X. Yang, G. Mao, Z. Jia, H. Zhou, T. Li, S. Qu, Z. Xu, Z. Huang, Y. Luo, T. Xie, J. Gu, S. Zhu, W. Yang, *Nature* **2021**, *591*, 66.

[19] A. Nojoomi, H. Arslan, K. Lee, K. Yum, *Nat. Commun.* **2018**, *9*, 3705.

[20] J. Li, B. Esteban-Fernandez de Avila, W. Gao, L. Zhang, J. Wang, *Sci. Rob.* **2017**, *2*, eaam6431.

[21] Y. Wu, J. K. Yim, J. Liang, Z. Shao, M. Qi, J. Zhong, Z. Luo, X. Yan, M. Zhang, X. Wang, R. S. Fearing, R. J. Full, L. Lin, *Sci. Rob.* **2019**, *4*, eaax1594.

[22] Y. Cheng, K. H. Chan, X. Q. Wang, T. Ding, T. Li, X. Lu, G. W. Ho, *ACS Nano* **2019**, *13*, 13176.

[23] Y. Kim, H. Yuk, R. Zhao, S. A. Chester, X. Zhao, *Nature* **2018**, *558*, 274.

[24] W. Hu, G. Z. Lum, M. Mastrangeli, M. Sitti, *Nature* **2018**, *554*, 81.

[25] T. Xu, J. Zhang, M. Salehizadeh, O. Onaizah, E. Diller, *Sci. Rob.* **2019**, *4*, eaav4494.

[26] Q. Ze, X. Kuang, S. Wu, J. Wong, S. M. Montgomery, R. Zhang, J. M. Kovitz, F. Yang, H. J. Qi, R. Zhao, *Adv. Mater.* **2020**, *32*, 1906657.

[27] X. Yang, W. Shang, H. Lu, Y. Liu, L. Yang, R. Tan, X. Wu, Y. Shen, *Sci. Rob.* **2020**, *5*, eabc8191.

[28] Y. Kim, G. A. Parada, S. Liu, X. Zhao, *Sci. Rob.* **2019**, *4*, eaax7329.

[29] R. Zhao, Y. Kim, S. A. Chester, P. Sharma, X. Zhao, *J. Mech. Phys. Solids* **2019**, *124*, 244.

[30] J. M. Silveyra, E. Ferrara, D. L. Huber, T. C. Monson, *Science* **2018**, *362*, eaao0195.

[31] Y. Zhang, F. Zhang, Z. Yan, Q. Ma, X. Li, Y. Huang, J. A. Rogers, *Nat. Rev. Mater.* **2017**, *2*, 17019.

[32] H. Yuk, B. Lu, S. Lin, K. Qu, J. Xu, J. Luo, X. Zhao, *Nat. Commun.* **2020**, *11*, 1604.

[33] C. Wang, C. Wang, Z. Huang, S. Xu, *Adv. Mater.* **2018**, *30*, 1801368.

[34] T. R. Ray, J. Choi, A. J. Bandodkar, S. Krishnan, P. Gutruf, L. Tian, R. Ghaffari, J. A. Rogers, *Chem. Rev.* **2019**, *119*, 5461.

[35] S. Xu, Z. Yan, K. I. Jang, W. Huang, H. Fu, J. Kim, Z. Wei, M. Flavin, J. McCracken, R. Wang, A. Badea, Y. Liu, D. Xiao, G. Zhou, J. Lee, H. U. Chung, H. Cheng, W. Ren, A. Banks, X. Li, U. Paik, R. G. Nuzzo, Y. Huang, Y. Zhang, J. A. Rogers, *Science* **2015**, *347*, 154.

[36] M. Han, L. Chen, K. Aras, C. Liang, X. Chen, H. Zhao, K. Li, N. R. Faye, B. Sun, J. H. Kim, W. Bai, Q. Yang, Y. Ma, W. Lu, E. Song, J. M. Baek, Y. Lee, C. Liu, J. B. Model, G. Yang, R. Ghaffari, Y. Huang, I. R. Efimov, J. A. Rogers, *Nat. Biomed. Eng.* **2020**, *4*, 997.

[37] K. I. Jang, K. Li, H. U. Chung, S. Xu, H. N. Jung, Y. Yang, J. W. Kwak, H. H. Jung, J. Song, C. Yang, A. Wang, Z. Liu, J. Y. Lee, B. H. Kim, J. H. Kim, J. Lee, Y. Yu, B. J. Kim, H. Jang, K. J. Yu, J. Kim, J. W. Lee, J. W. Jeong, Y. M. Song, Y. Huang, Y. Zhang, J. A. Rogers, *Nat. Commun.* **2017**, *8*, 15894.

[38] J. D. Servaites, M. A. Ratner, T. J. Marks, *Energy Environ. Sci.* **2011**, *4*, 4410.

[39] M. A. Green, A. Ho-Baillie, H. J. Snaith, *Nat. Photonics* **2014**, *8*, 506.

[40] X. Qian, Y. Zhao, Y. Alsaid, X. Wang, M. Hua, T. Galy, H. Gopalakrishna, Y. Yang, J. Cui, N. Liu, M. Marszewski, L. Pilon, H. Jiang, X. He, *Nat. Nanotechnol.* **2019**, *14*, 1048.

[41] A. Lamoureux, K. Lee, M. Shlian, S. R. Forrest, M. Shtein, *Nat. Commun.* **2015**, *6*, 8092.

[42] W. Wu, Z. L. Wang, *Nat. Rev. Mater.* **2016**, *1*, 16031.